# The 1998 Mw 5.7 Zhangbei-Shangyi earthquake revisited: a buried thrust fault revealed with interferometric synthetic aperture radar

Geochemistry Geophysics Geosystems G3
AN ELECTRONIC JOURNAL OF THE EARTH SCIENCES
Published by AGU and the Geochemical Society

*Article*
Volume 9, Number 4
17 April 2008
Q04026, doi:10.1029/2007GC001910
ISSN: 1525-2027

Click Here for Full Article

# The 1998 $M_w$ 5.7 Zhangbei-Shangyi (China) earthquake revisited: A buried thrust fault revealed with interferometric synthetic aperture radar

**Zhenhong Li**
*COMET, Department of Civil, Environmental and Geomatic Engineering, University College London, Gower Street, London WC1E 6BT, UK*

*Now at Department of Geographical and Earth Sciences, University of Glasgow, Glasgow G12 8QQ, UK (zhenhong.li@ges.gla.ac.uk)*

**Wanpeng Feng and Zhonghuai Xu**
*Institute of Geophysics, China Earthquake Administration, Beijing 100081, China*

**Paul Cross**
*COMET, Department of Civil, Environmental and Geomatic Engineering, University College London, Gower Street, London WC1E 6BT, UK*

**Jingfa Zhang**
*Institute of Crustal Dynamics, China Earthquake Administration, Beijing 100085, China*

[1] The 1998 $M_w$ 5.7 Zhangbei-Shangyi (China) earthquake is the largest to have occurred in northern China since the large 1976 $M_s$ 7.8 Tangshan earthquake. Due to its proximity to Beijing, the capital of China, it has therefore gained a lot of attention. A great number of studies have been conducted using seismic and geodetic data, but few are able to identify conclusively the orientation of the primary fault plane for this earthquake. In this paper, two independent ERS synthetic aperture radar interferograms are used to determine precisely the location and magnitude of coseismic surface displacements ($\sim$11 cm in the radar line of sight). Modeling the event as dislocation in an elastic half-space suggests that the earthquake is associated with a buried shallow NNE-SSW oriented thrust fault with a limited amount of lateral displacement, which is consistent with seismic intensity distribution and aftershock locations.

**Components:** 6156 words, 7 figures, 2 tables.

**Keywords:** InSAR; earthquake; Zhangbei; aftershock.

**Index Terms:** 1240 Geodesy and Gravity: Satellite geodesy: results (6929, 7215, 7230, 7240); 1209 Geodesy and Gravity: Tectonic deformation (6924); 1243 Geodesy and Gravity: Space geodetic surveys.

**Received** 23 November 2007; **Revised** 18 February 2008; **Accepted** 29 February 2008; **Published** 17 April 2008.

Li, Z., W. Feng, Z. Xu, P. Cross, and J. Zhang (2008), The 1998 $M_w$ 5.7 Zhangbei-Shangyi (China) earthquake revisited: A buried thrust fault revealed with interferometric synthetic aperture radar, *Geochem. Geophys. Geosyst.*, *9*, Q04026, doi:10.1029/2007GC001910.

## 1. Introduction

[2] On 10 January 1998 at 03:50 (UTC), a $M_w$ 5.7 earthquake struck the Zhangbei-Shangyi region of northwestern Hebei Province, China, causing 49 fatalities, 11,439 serious injuries and rendering ~44,000 homeless. The direct economic loss was estimated to be about $300 million (http://www.eq-he.gov.cn/10/10-4/10-4-2.htm, accessed on 1 October 2007). The Zhangbei-Shangyi earthquake occurred in a Cenozoic uplifting region covered with 2000 km$^2$ of basalt [*Diao et al.*, 2001]. To the southwest of the earthquake region is the Ordos basin (Figure 1) where a regional GPS network was established in the early 1990s. The GPS network has been subsequently resurveyed in a campaign mode with an interval of 1~2 years. GPS observations spanning the period from 1991 to 2001 suggest coherent east-southeastward movement at rates of 2 to 8 mm/a in the direction of N120°–140°E with respect to the relatively stable Eurasian plate [*Wang et al.*, 2001] (Figure 1). The Ordos basin is a relatively stable geological block surrounded by seismically active deformation zones. There have been no moderate or large earthquakes ($M > 4.0$) and only a few small earthquakes recorded in the last 2500 years within the Ordos block. By contrast, the surrounding deformation zones are very active with 15 strong earthquakes ($7.0 < M \leq 8.5$) and more than 35 moderately strong earthquakes ($6.0 < M \leq 7.0$) having occurred in the past 2500 years [*Deng et al.*, 1999].

[3] On the basis of seismic intensity distribution, aftershock locations, the focal mechanism, and the directions of fallen chimneys and gate pillars, *Lin et al.* [1999] reported a thrust fault striking NNE and dipping 40° to 50° northwest with a large right-lateral displacement component. Using the far-field and near-field digital seismic records, *Gao et al.* [2002] argued that the Zhangbei-Shangyi event consisted of one main left-lateral strike-slip rupture plane (NWW striking, NNE dipping) and two right-lateral strike-slip secondary rupture planes (NNE striking). A more recent study using near-field seismic records suggested that the earthquake occurred on a NW striking fault [*Lai et al.*, 2007].

[4] In the past two decades, interferometric synthetic aperture radar (InSAR) has proved a powerful technique for mapping deformation of the Earth's surface caused by earthquakes with tens-of-meters spatial resolution [*Massonnet and Feigl*, 1998]. Wang and his colleagues were the first to apply the InSAR technique to mapping the Zhangbei-Shangyi earthquake [*Wang et al.*, 2000; *Zhang et al.*, 2001, 2002; *Shan et al.*, 2002]. Using three-pass InSAR with an ERS descending interferogram from one tandem pair collected before the earthquake plus one image after the event, they observed a coseismic signal of up to 25 cm for this small earthquake and suggested that this fault was a SEE striking thrust fault dipping SW with a large right-lateral displacement component. Moreover, they claimed a magnitude ($M_w$) of 6.2, which is much greater than the magnitude from the Global Centroid Moment Tensor (GCMT) catalog ($M_w$ = 5.7).

[5] Since the focal mechanism solutions differ from one method to another, the fault type for the Zhangbei-Shangyi earthquake is still unclear. In this paper, an attempt is made to use two independent two-pass interferograms to determine precisely the fault location and its coseismic signals, and then to understand better its mechanism.

## 2. Interferometric Processing Strategy

[6] The ERS coverage of the Zhangbei-Shangyi earthquake region is shown in Figure 1. Repeated radar acquisitions are available from two adjacent descending tracks (satellite moving south), tracks 032 and 304 (Table 1). The InSAR data were processed from level 0 (raw data) products using the JPL/Caltech ROI_PAC software (version 2.3) [*Rosen et al.*, 2004]. Effects of topography were removed from the interferograms using a 3-arc-second (~90 m) digital elevation model (DEM) produced by the Space Shuttle Radar Topography Mission (SRTM) [*Farr et al.*, 2007].

[7] Figure 2 shows the two independent interferograms used in this study. Precise satellite orbits from Delft University [*Scharroo and Visser*, 1998] were employed to process the pair from track 304 (T304D hereafter, Figure 2a). T304D has a small baseline, and the typical topographic errors in the SRTM DEM (~8.7 m in Eurasia [*Farr et al.*, 2007]) might lead to a range change error of 0.11 cm (Table 1), which is two orders of magnitude smaller than the coseismic signal (~11 cm, Figure 2c). Therefore, for the T304D pair, the topographic contribution can be considered negligible.

[8] Since no precise orbit was available for the ERS-1 image collected on 8 October 1997, predicted orbits contained in the leader (header) files were used in interferometric processing for the pair from track 032 (T032D hereafter) and more than

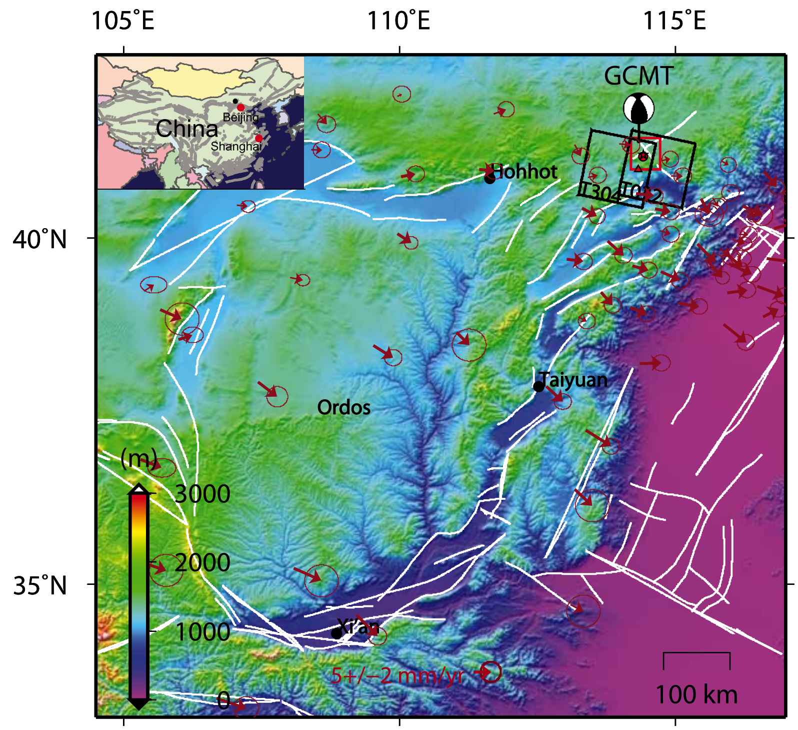


**Figure 1.** Topographic map of the Ordos basin covering the 1998 Zhangbei-Shangyi earthquake. Inset shows the location of the earthquake (indicated by a solid black point). The focal mechanism is from the Global Centroid Moment Tensor (GCMT) catalog. White lines show previously mapped faults [*Deng et al.*, 2003]. Red solid rectangles show the 46 × 46 km area around Zhangbei-Shangyi shown in Figures 2a, 2b, 3, 5a, 7, and S1; black solid lines delimit the extents of the InSAR data used for this study; brown vectors represent GPS velocities relative to the relatively stable Eurasian plate with ellipses denoting a region of 1$\sigma$ error, which are from *Wang et al.* [2001].

40 fringes were observed across the track (not shown). Given the ERS swath width of 100 km, these orbital ramps could result from a 11 m horizontal baseline error or a 27 m vertical baseline error [*Li et al.*, 2004; *Sibthorpe*, 2006], which is of the order for the accuracy of the predicted orbits for ERS-1/2 (i.e., ~25 m) [*Closa*, 1998]. Because the coseismic signal is localized, the orbital ramp can be removed using a best fit plane and the flattened interferogram is shown in Figure 2b. T032D has a long baseline of 440 ± 25 $\sqrt{2}$ m, and topographic errors could be up to ~1.2 cm. Phase shifts are observed in the epicenter region (indicated by a black dashed eclipse) in T032D. On closer inspection of the SRTM DEM and satellite images (including SAR and Google images), it is found that these signals coincide with topography (e.g., riverbanks) with moderately steep slopes (see the topography profile in Figure 2c), and thus it appears that the phase shifts in T032D are likely to be due to uncertainties in the SRTM DEM, although the possibility of phase unwrapping errors and atmospheric effects cannot be ruled out without additional information (e.g., multiinterfero-

**Table 1.** ERS SAR Data Used in the InSAR Analysis

| | Track | Frame | Date 1 | Orbit 1 | Date 2 | Orbit 2 | $B_\perp$,[a] m | $h_a$,[b] m | $\sigma$,[c] cm | $\theta$,[d] deg |
|---|---|---|---|---|---|---|---|---|---|---|
| Descending | 304 | 2781 | 23 Sep 1997 | 12683(ERS-2) | 26 May 1998 | 16190(ERS-2) | 41 | 220 | 0.11 | 20.4 |
| Descending | 032 | 2778 | 8 Oct 1997 | 32585(ERS-1) | 22 Jan 1998 | 14415(ERS-2) | 440 | 20 | 1.20 | 24.5 |

[a] $B_\perp$ is the perpendicular baseline, which is the component of the orbital separation perpendicular to the radar line of sight.
[b] The parameter $h_a$ is the altitude of ambiguity or the change of altitude corresponding to a topographic fringe. The higher this number, the lower the sensitivity of the displacement measurement to residual topographic errors.
[c] Range change errors in the line of sight due to the topographic uncertainty of SRTM DEM (typically 8.7 m for Eurasia [*Farr et al.*, 2007]).
[d] The parameter $\theta$ is the incidence angle at the location of the peak surface displacement.

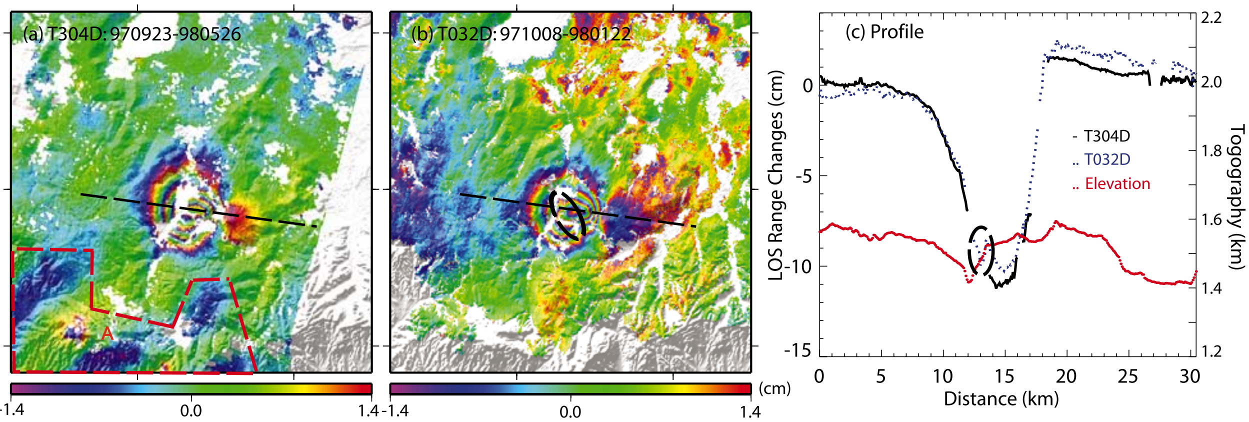


**Figure 2.** (a) Interferogram T304D: 970923–980526. The region indicated by orange red dashed lines (also labeled A) was masked in slip modeling due to atmospheric effects. (b) Interferogram T032D: 971008–980122. (c) Profiles of interferograms T304D and T032D, and topography. Note: (1) The interferograms in Figures 2a and 2b are wrapped so that each color cycle from violet to red to violet represents an increase of 2.8 cm in the range to the satellite. (2) The straight black dashed lines in Figures 2a and 2b indicate the profiles shown in Figure2c. (3) Negative LOS range changes imply that the surface moves toward the satellite; that is, the pixel exhibits uplift in the LOS direction. (4) It is believed that the differences in the observed deformation patterns in Figures 2a and 2b can be mainly accounted for by two factors: the difference in the incidence angles of the two tracks (Table 1) and atmospheric effects. (5) Dashed ellipses in Figures 2b and 2c imply phase shifts most likely due to SRTM DEM errors (see text).

grams for pair-wise logic assessment [*Massonnet and Feigl*, 1998], or GPS, NASA MODIS and ESA MERIS data for atmospheric correction [*Li et al.*, 2005, 2006a, 2006b]). Increasing water levels also result in a greater surface of water during the summer than the winter, which in turn leads to more incoherent pixels in the "summer" pair (T304D: September–May).

[9] A profile of unwrapped phase across the T304D interferogram gives a maximum range change of about 11.0 cm in the radar line of sight (LOS) (Figure 2c). Assuming that most of the motion was vertical at the maximum, this corresponds to 11.9 cm of uplift. Note that Wang and his colleagues observed a coseismic signal of up to 25 cm using a three-pass InSAR technique [*Wang et al.*, 2000; *Zhang et al.*, 2001, 2002; *Shan et al.*, 2002], which is almost twice as large. For the purpose of validation, the three ERS images used by Wang and his colleagues were reprocessed using the three-pass InSAR technique in this study, and the resultant interferogram agrees well with the 2-pass pair with a RMS difference of 1.1 cm and suggests a maximum LOS range change of ~11.0 cm (Figure S1).[1] Moreover, it is clear in Figure 2c that the two independent T304D and T032D profiles are in a good agreement with a mean difference (T032D–T304D) of 0.3 cm, a RMS difference of 0.6 cm, and a peak difference of ~1.9 cm, providing strong confidence in our InSAR results.

[10] The difference between the incidence angles of the peak surface displacements in T032D and T304D is as small as 4.1 degrees (Table 1); additional uncertainties due to topographic errors, phase unwrapping and/or atmospheric effects (e.g., that indicated by black dashed eclipses in Figure 2b) are expected if the T032D pair is used alongside T304D in the inversion. Hence, in this paper the T032D interferogram is only used for validation.

## 3. Determining Fault Parameters Using InSAR

[11] A comparison between Figures 2a and 2b reveals that there are some short-wavelength atmospheric effects (or atmospheric ripples, likely to be caused by gravity waves) in the southwest corner of the T304D interferogram (labeled A). They can be observed more easily in a wider region, e.g., Figure S2a. These signals would make it difficult to infer the mechanisms of such a small earthquake [*Lohman and Simons*, 2005] and were therefore masked during further modeling. The T304D interferometric phase were then subsampled using a quadtree decomposition algorithm [*Jónsson et al.*,

[1] Auxiliary materials are available in the HTML. doi:10.1029/2007GC001910.

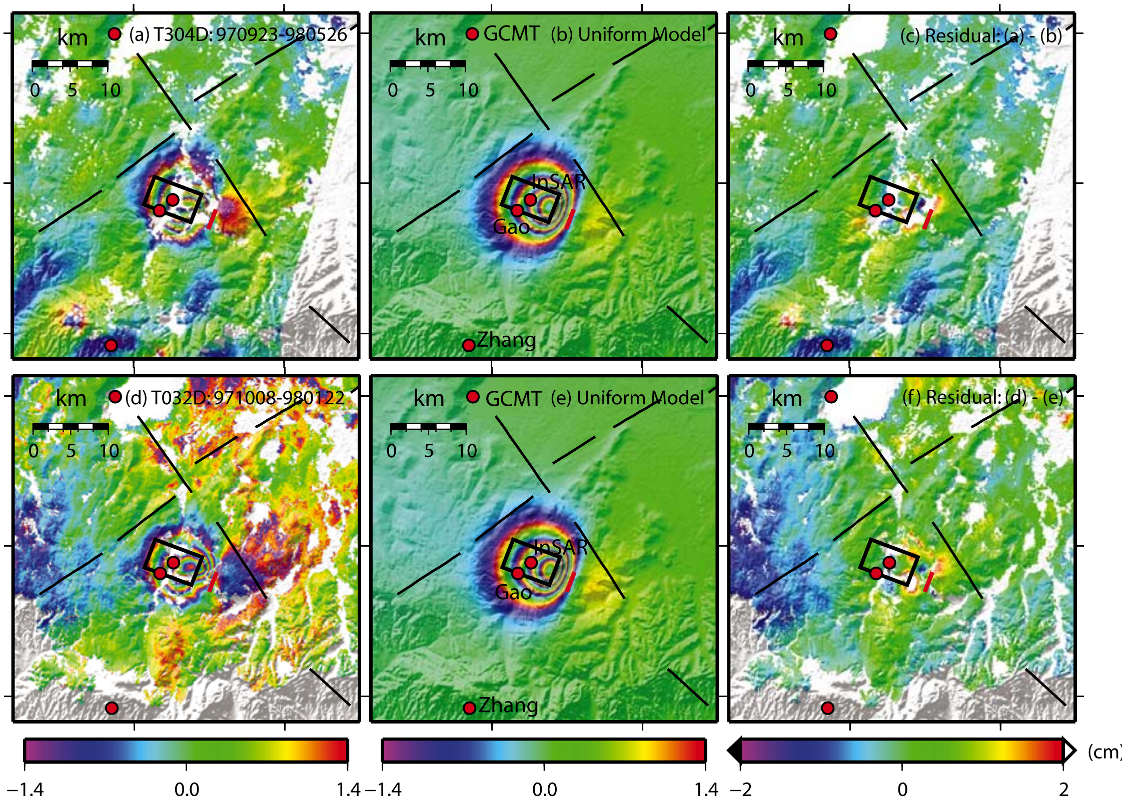


**Figure 3.** Observed, model, and residual interferograms superimposed on a SRTM DEM. (a) T304D interferogram (wrapped): 970923–980526. (b) T304D WDM (wrapped). (c) T304D WDM residual interferogram. (d) T032D interferogram (wrapped): 971008–980122. (e) T032D WDM (wrapped). (f) T032D WDM residual interferogram. Note: (1) The observed and model interferograms are wrapped so that each color cycle from violet to red to violet represents an increase of 2.8 cm in the range to satellite, while the residual one is not wrapped due to its relatively small magnitude. (2) Black lines show previously mapped faults [*Xu et al.*, 1998], and red circles indicate the centroid locations from GCMT, Gao [*Gao et al.*, 2002], Zhang [*Zhang et al.*, 2001], and this study (labeled InSAR), respectively. (3) Black rectangles show the map view projections of the west dipping fault plane, and dashed red lines indicate the fault rupture projected on the surface that would be expected in the black rectangles if the fault broke the surface.

2002], a technique which concentrates sampling in areas of high phase gradients, thus reducing the number of data points to be modeled from ~15,000 to just 529.

### 3.1. Uniform Slip Modeling

[12] To determine the source mechanism for the 1998 Zhangbei-Shangyi earthquake from the T304D interferogram, interferometric phase was modeled with uniform slip on a rectangular dislocation in an elastic half-space using the formulation of *Okada* [1985]. An elastic shear modulus of $3.23 \times 10^{10}$ Pa and a Poisson ratio of 0.25 were used. Two inversions were performed on the T304D interferogram: a West-Dipping Model (WDM) constrained the strike angle to be within 80° (167°–247°) of the west dipping nodal plane determined by GCMT, and a East-Dipping Model (EDM) to be within 80° (310°–30°) of the east dipping nodal plane. Fault parameters (including strike, slip, length, location, minimum and maximum depth) were determined by minimizing the squared misfits between the observed and the predicted range changes in the LOS direction using a nonlinear downhill simplex algorithm with multiple Monte Carlo restarts to avoid local minima [e.g., *Harris and Segall*, 1987; *Segall and Harris*, 1987; *Clarke et al.*, 1997; *Wright et al.*, 1999]. To determine parameter errors for the nonlinear downhill simplex inversion, a Monte Carlo bootstrap simulation using correlated noise was used [e.g., *Cervelli et al.*, 2001; *Jónsson*, 2002; *Wright et al.*, 2003; *Funning et al.*, 2005]. First, a best fit 1-D covariance function was estimated using a far-field

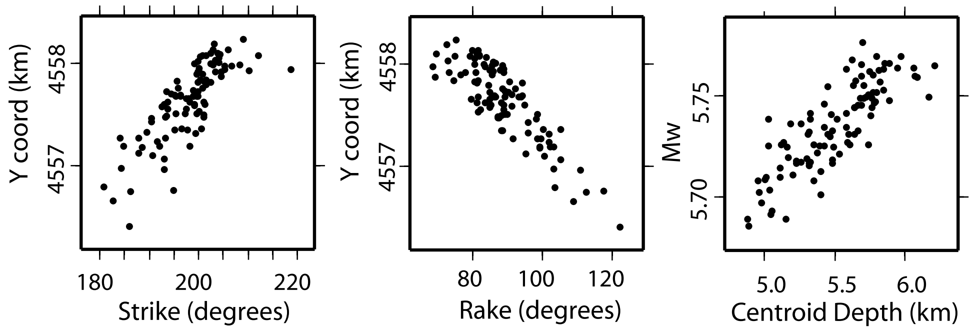


**Figure 4.** Model parameter trade-offs for uniform-slip model. Each of the 100 dots is the best fit solution for one data set to which Monte Carlo, correlated noise has been added (see text).

area of the interferogram where there is no deformation signal from the earthquake. Second, a full variance-covariance matrix was constructed for the sampled data points, assuming that the noise structure was isotropic and identical across the image. Third, 100 sets of random correlated noise were simulated using the full variance-covariance function and then added to the sampled data points to create 100 perturbed data sets. Finally, the inversion procedure was applied to each of these data sets and the distribution of best fitting solutions obtained provides information on parameter errors and their trade-offs.

[13] The WDM converged easily to a strike of 200.8 degrees. The model interferogram is shown in Figure 3b and its residuals in Figure 3c. It is clear that the WDM produces a first-order fit to the observed deformation pattern and fixes the top of the fault at a depth of ~2.3 km, consistent with the absence of a fault scarp at the surface. The WDM has a small root mean square (RMS) misfit to the data (6.2 mm for the subsampled data points and 4.4 mm for all the data points). Note that the RMS misfits include the contributions from the uncertainty in the InSAR measurements which was suggested to be 2.0 mm by the abovementioned variance-covariance estimation process. On the basis of the Monte Carlo simulation of correlated noise, several strong trade-offs between different model parameters are observed: such as between the strike and the y-coordinate, between the rake and the y-coordinate, and between the moment magnitude and the centroid depth (Figure 4). By contrast, the EDM did not converge even after 1000 Monte Carlo restarts, i.e., the inversion finished only when the number of Monte Carlo restarts was beyond its threshold. Examination of the inversion outputs revealed that it repeatedly hit the bounds of the strike angle. When the model constrained the strike angle to lie in a much wider range of 190°–490°, it eventually converged to the west dipping nodal plane (instead of the east dipping one). This indicates that the EDM is not capable of reproducing the first-order pattern of observed ground deformation.

[14] It is worth mentioning that an independent inversion was performed using both T032D and T304D interferograms in this study with Particle Swarm Optimization (PSO) [*Eberhart and Kennedy*, 1995] employed to find the global minima. Compared to the downhill simplex algorithm, much looser constraints were set: the strike angle was constrained to be within 5° to 355°, dip to be within 0.1° to 89.9° and rake to be within −179° to 179°. The PSO was restarted 100 times with initial model parameters produced by a random function. The PSO solution was similar to the downhill simplex solution with the strike angle converging at 199.0 ± 15.0 degrees. Therefore, the uniform slip modeling results are strongly in favor of the WDM.

[15] As can be seen in Figures 3d–3f, the coseismic signals observed in the independent T032D interferogram can also be modeled effectively by the WDM with a RMS misfit of 5.6 mm (Table 2); their residual images are dominated by atmospheric noise (Figure 3f). This provides additional strong supporting evidence for the uniform modeling results. Note that there are some observable differences between the T304 WDM and the T032 WDM interferograms (i.e., Figures 3b and 3e). This is entirely because of the differences in the incidence angles of the two adjacent descending tracks (Table 1).

[16] Figure 5a shows the seismic intensity map (dark gray lines) based on surface observations [*Diao et al.*, 2001] as well as the distribution of the 178 aftershocks collected during the period

**Table 2.** Source Parameters and Their 1$\sigma$ Confidence Limits From Various Source Models

| Model[a] | Data | Strike, Deg | Dip, deg | Rake, deg | Longitude,[b] deg | Latitude,[b] deg | Centroid Depth, km | Slip, m | Length, km | Width, km | Moment Magnitude ($M_w$) | RMS Misfit[c], mm | |
|---|---|---|---|---|---|---|---|---|---|---|---|---|---|
| | | | | | | | | | | | | T304D | T032D |
| GCMT | seismic | 207 | 54 | 135 | 114.34 | 41.34 | 15.0 | | | | 5.7 | | |
| | | 327 | 55 | 46 | | | | | | | | | |
| Gao | aftershock | | | | 114.42 | 41.13 | | | | | | | |
| Zhang | InSAR | 95 | 30 | 105.95 | 114.350 | 40.967 | 7.5 | 0.728 | 12 | 14 | 6.2 | | |
| WDM | InSAR | 200.8 ± 6.4 | 42.7 ± 3.6 | 85.9 ± 10.2 | 114.440 ± 0.4 km | 41.143 ± 0.4 km | 5.4 ± 0.3 | 0.41 ± 0.04 | 4.0 ± 0.2 | 9.0 ± 0.8 | 5.72 | 4.4 | 5.6 |

[a] GCMT, Global Centroid Moment Tensor (GCMT); Gao, *Gao et al.* [2002]; Zhang, *Zhang et al.* [2001]; WDM, West-Dipping Model in this study.
[b] The location for the WDM is defined as the center of the uniform slip plane projected vertically to the surface.
[c] RMS misfit values were calculated using all the data points.

between 12 February 1998 and 28 February 1998 [*Lai et al.*, 2007]. The WDM, projected onto the high-intensity zone, shows a good agreement with the seismic intensity map (Figure 5a). There is no obvious orientation trend to the aftershock locations, but 164 out of 178 aftershocks are located to the west of the fault rupture projected on the surface (red dashed line in Figure 5a), which is consistent with the WDM. Moreover, their depth distribution also clearly indicates the aftershock zone has a moderate westward dip (Figure 5b).

[17] A final indirect test of the validity of the WDM model can be made by simulating the model(s) suggested by *Zhang et al.* [2001] and calculating their residuals, as this previous InSAR study proposed a completely different focal mechanism solution. It is clear that the model(s) in the work of *Zhang et al.* [2001] cannot reproduce the coseismic signals for the earthquake, as evidenced by their overestimated magnitudes and also their imprecise locations (Figure S2). Since very limited information on interferometric processing is available in the cited references [i.e., *Wang et al.*, 2000; *Zhang et al.*, 2001, 2002; *Shan et al.*, 2002], the reason for their overestimate of the coseismic signals remains unknown. However, it appears that geocoding may be an issue in their interferometric processing.

[18] Figure 3 shows that the GCMT earthquake location differs from our InSAR result by 23.4 km, but the latter is in agreement with the precise location derived from near-field digital seismic records [*Gao et al.*, 2002] (labeled Gao) with a small distance difference of 2.2 km, indicating that InSAR data is able to provide invaluable information to precisely locate earthquakes.

## 3.2. Distributed Slip Modeling

[19] Once the orientation of the fault plane has been determined, the model can be further refined by solving for the distribution of slip on the fault. Assuming the fault geometry for a NNE-SSW fault plane determined in the uniform slip modeling, we extended the fault plane along strike and downdip by increasing its total length to 20 km and downdipwidth to 18 km, and then divided the fault into 20 by 18 subfaults each measuring 1 km by 1 km. The best fitting values of strike-slip and dip-slip motion for each subfault were solved in a least squares sense while Laplacian smoothing and a nonnegative least squares algorithm were employed to prevent unphysical oscillatory slip [e.g., *Harris and Segall*, 1987; *Segall and Harris*,

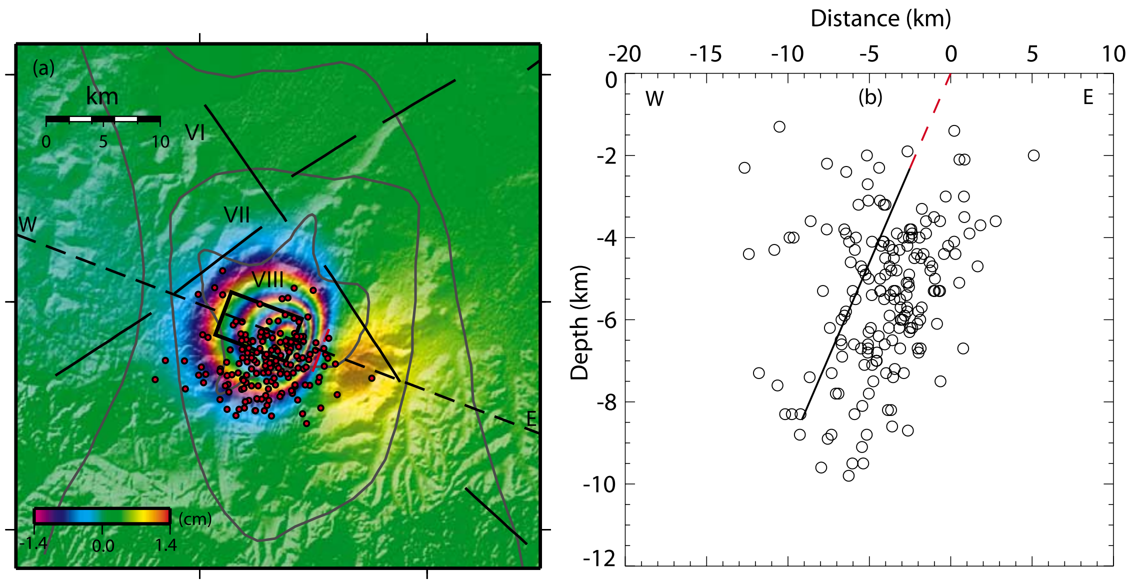


**Figure 5.** Aftershock locations for the 1998 Zhangbei-Shangyi earthquake superimposed on the WDM synthetic interferogram. (a) Locations of the 178 aftershocks (indicated by red solid circles), determined by [*Lai et al.*, 2007]. Black lines show previously mapped faults [*Xu et al.*, 1998], and the dashed gray lines indicate isoseismals VI, VII, and VIII [*Diao et al.*, 2001]. (b) Cross section along the line W-E in Figure 5a. The black solid line is the WDM fault plane determined in this study, and the red dashed line joins the top of the WDM fault to the fault rupture projected on the surface.

1987; *Bro and Jong*, 1997; *Wright et al.*, 2003; *Funning et al.*, 2005]. There is a trade-off between the RMS misfit and the solution roughness, a dimensionless quantity defined to be the mean absolute Laplacian of the slip model. By plotting RMS misfit against solution roughness, the weighting of the Laplacian smoothing (i.e., 300) was chosen to given a solution that had both low misfit and roughness (Figure S3).

[20] The slip distribution obtained is shown in Figure 6, which is elliptical in shape. Slip is concentrated within the upper 8 km of the fault, peaking at 0.55 m at a depth of 4–5 km, corresponding to the center of the best fit uniform fault. The maximum slip in the top 1 km (i.e., near surface) is 0.03 m and may be too small to be detected, which is consistent with the absence of a fault scarp at the surface. To determine the level of uncertainty in the slip estimates, the slip inversion was applied to 100 perturbed data sets generated using realistic correlated noise as for the uniform models. The standard deviation of the slip on each subfault gives a measure of the error on each slip estimate (Figure S4). It is clear that the errors increase with depth to a maximum of 0.05 m at a depth of 6–7 km.

[21] To assess the degree of detail that is resolvable with the distributed slip model, the resolution matrix was used to estimate the spatial resolution at the location of any subfault in the model (e.g., *Biggs et al.*, 2006; *Funning et al.*, 2005). The resulting horizontal and vertical resolution lengthscales are given in Figures S5a and S5b, respectively, where the resolution lengthscale at each element is defined to be the number of elements in the horizontal and vertical direction for which the value in the resolution matrix is greater than $1/e$ of the maximum. The horizontal resolution is 3 km and the vertical resolution 5 km at the depth of peak slip (i.e., 4–5 km), while they decrease to 6 km and 7 km, respectively, at the bottom depth of the best fit uniform model (i.e., 8–9 km). The latter two are comparable to the dimensions of the fault, indicating there is only a marginal improvement of the variable-slip model over the simpler uniform one, which is within our expectation for earthquakes of this size and smaller [*Biggs et al.*, 2006]. This is supported by the fact that the distributed slip model only shows a marginally improved fit, with an RMS misfit of 4.3 mm for all the data points (Figure 7) against the uniform slip inversion (4.4 mm, Figure 3).

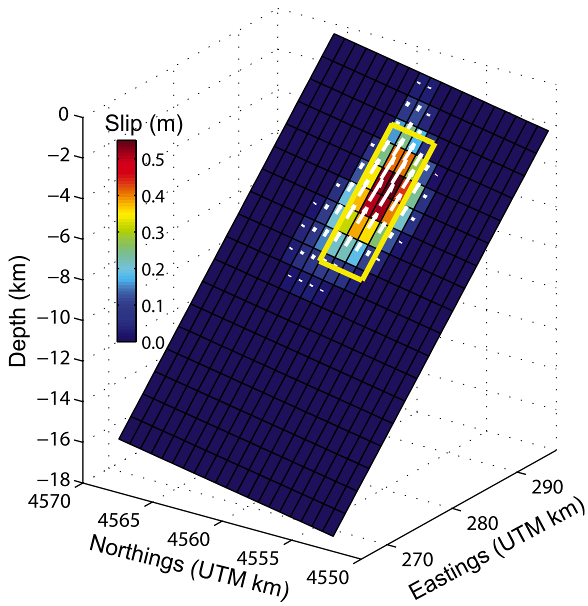


**Figure 6.** Slip distribution for a fault plane 20 km long, 18 km downdipwide, and dipping 42.7°. Horizontal coordinates are in kilometers, projected into Universal Transverse Mercator (UTM) coordinates (Zone 50N). Note: (1) The yellow rectangle represents the extent and location of the best fit uniform fault plane. (2) White arrows indicate slip vectors ($\geq$ 0.03 m) of the 1 km $\times$ 1 km subfaults.

[22] As shown in Figure 7, however, both the width and the downdipextent of the slipping area are in a good agreement with those of the best fit uniform fault (indicated by the yellow rectangle). Comparisons between Figures 3 and 7 reveal that the pattern of the distributed slip model does appear to be closer to that of the observed signals than the best fit uniform model, particularly in the region along the fault rupture projected on the surface (indicated by dashed red lines). Moreover, the distributed slip model seismic moment of 4.72 $\times$ $10^{17}$ Nm agrees closer to the GCMT moment (4.48 $\times$ $10^{17}$ Nm) than the uniform model moment (4.82 $\times$ $10^{17}$ Nm), suggesting that slip has been removed from areas that did not require it in the previous case.

## 4. Discussion and Conclusions

[23] Previous seismological and geodetic observations of the 1998 Zhangbei-Shangyi earthquake were ambiguous, suggesting the earthquake could have occurred on a NNE striking right-lateral fault plane, a NWW striking left-lateral fault plane, or a SEE striking thrust fault plane. Initial InSAR observations showed an unreasonably large coseismic signal of up to 25 cm for such a small earthquake [*Diao et al.*, 2004]. By contrast, two independent interferograms were constructed in this study using ERS data from two adjacent tracks, and both provide a maximum coseismic signal of ~11 cm for this earthquake.

[24] In order to determine the fault parameters of a uniform slip model on a rectangular dislocation in an elastic half-space, two optimization algorithms were employed: downhill simplex and Particle Swarm Optimization (PSO). Both results are strongly in favor of a west dipping fault plane with a strike angle of 200.8 ± 6.4 degrees, which is also

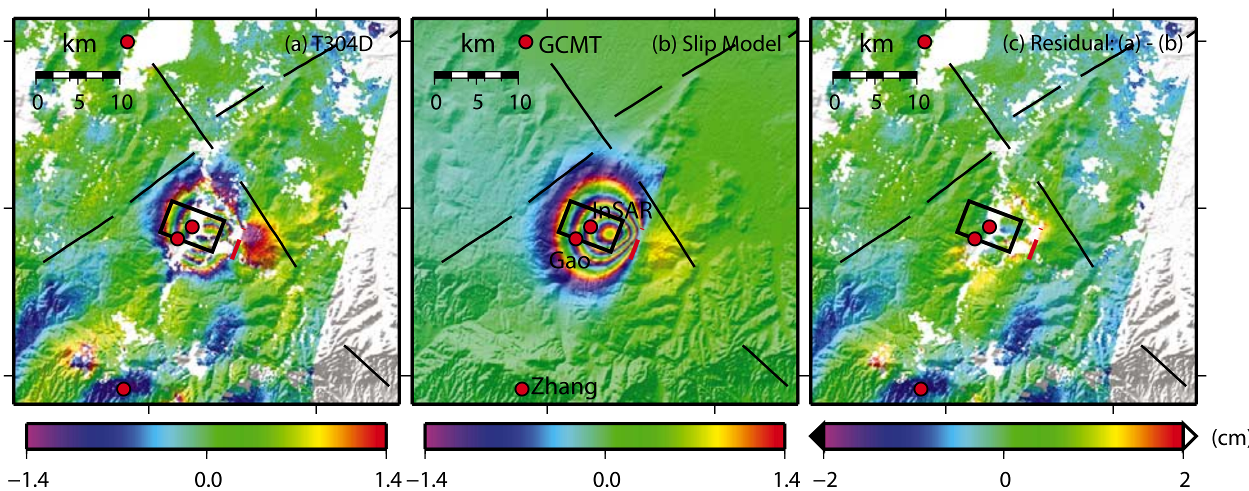


**Figure 7.** The T304D, distributed slip model, and residual interferograms superimposed on a SRTM DEM. (a) The T304D interferogram (wrapped). (b) The distributed slip model (wrapped). (c) The residual interferogram. Panels as in Figures 3a–3c.

evidenced by the aftershocks collected in the following month after the earthquake. In contrary to previous seismological solutions, this InSAR study suggests that this earthquake was due to a buried thrust fault with a very limited amount of lateral displacement component. A further distributed slip model suggests that the peak slip of 0.55 m is located at a depth of 4–5 km.

[25] Figures 3, 6 and 7 show that the GCMT earthquake location differs from the results from near-field digital seismic records and InSAR measurements by about 23 km and 24 km, respectively, but the latter two are in agreement with each other, highlighting the location uncertainties in the GCMT catalog and the potential of InSAR techniques for precise earthquake location [*Lohman and Simons*, 2005]. The InSAR-derived magnitude is slightly larger than that from seismic data, which is consistent with the results reported by *Lohman and Simons* [2005]. Since the T304D interferogram spanned a long time interval and potentially included interseismic deformation, postseismic deformation and aftershocks (except for the main shock), the inferred geodetic moment should be viewed as a sum of these movements. The differences in magnitude estimates are expected to decrease with increasing time resolution of InSAR data.

## Acknowledgments

[26] This work has been carried out within the NERC Earth Observation Centre of Excellence: COMET. Part of this research was carried out at IGP/CEA (funded by Project DQJB0601). We thank A. Sibthorpe for useful discussions, Tim Wright, Gareth Funning, and Juliet Biggs for the slip inversion. We are grateful to the associate editor, an anonymous reviewer, and Gareth Funning (once again) for thoughtful and thorough reviews, which have significantly improved the manuscript. We thank JPL/Caltech for the use of the ROI_PAC software to generate our interferograms [*Rosen et al.*, 2004]. We are grateful to the European Space Agency for providing ERS data to project C1P.3336. The GMT mapping software [*Wessel and Smith*, 1998] was used to prepare Figures 1, 2a, 2b, 3, 4, 5a, 7, S1, and S2 in the paper.

## References

Biggs, J., E. Bergman, B. Emmerson, G. J. Funning, J. Jackson, B. Parsons, and T. J. Wright (2006), Fault identification for buried strike-slip earthquakes using InSAR: The 1994 and 2004 Al Hoceima, Morocco earthquakes, *Geophys. J. Int.*, *166*, 1347–1362, doi:10.1111/j.1365-246X.2006.03071.x PubMed.

Bro, R., and S. D. Jong (1997), A fast non-negativity-constrained least squares algorithm, *J. Chemometr.*, *11*, 393–401, doi:10.1002/(SICI)1099-128X(199709/10)11:5<393::AID-CEM483>3.0.CO;2-L.

Cervelli, P., M. H. Murray, P. Segall, Y. Aoki, and T. Kato (2001), Estimating source parameters from deformation data, with an application to the March 1997 earthquake swarm off the Izu Peninsula, Japan, *J. Geophys. Res.*, *106*, 11,217–11,237, doi:10.1029/2000JB900399.

Clarke, P. J., D. Paradissis, P. Briole, P. C. England, B. E. Parsons, H. Billiris, G. Veis, and J.-C. Ruegg (1997), Geodetic investigation of the 13 May 1995 Kozani-Grevena (Greece) earthquake, *Geophys. Res. Lett.*, *24*, 707–710, doi:10.1029/97GL00430.

Closa, J. (1998), The influence of orbit precision in the quality of ERS SAR interferometric data, *Doc. ES-TN-APP-APM-JC01*, Eur. Space Agency, Paris. (Available at http://earth.esa.int/rootcollection/sysutil/ORB_QL.html)

Deng, Q. D., S. P. Cheng, W. Min, G. Z. Yang, and D. W. Ren (1999), Discussion on Cenozoic tectonics and dynamics of Ordos Block, (in Chinese), *J. Geomech.*, *5*, 13–21.

Deng, Q., P. Zhang, Y. Ran, X. Yang, W. Min, and Q. Chu (2003), Basic characteristics of active tectonics of China, *Sci. China, Ser. D*, *46*, 356–372.

Diao, G., H. Cai, and J. Diao (2001), The macrointensity of Zhangbei Ms 6.2 earthquake in 1998, *N. China Earthquake Sci.*, *19*, 23–30.

Diao, G., S. Zhang, H. Cai, and Y. Zhang (2004), The cause of surface displacements in the Zhangbei earthquake region, *Chin. Sci. Bull.*, *49*, 1214–1216, doi:10.1360/04wd0033.

Eberhart, R. C., and J. Kennedy (1995), A new optimizer using particle swarm theory, paper presented at Sixth International Symposium on Micromachine and Human Science, Inst. of Electr. and Electron. Eng., Nagoya, Japan.

Farr, T. G., et al. (2007), The Shuttle Radar Topography Mission, *Rev. Geophys.*, *45*, RG2004, doi:10.1029/2005RG000183.

Funning, G. J., B. Parsons, T. J. Wright, J. A. Jackson, and E. J. Fielding (2005), Surface displacements and source parameters of the Bam (Iran) earthquake from Envisat advanced synthetic aperture radar imagery, *J. Geophys. Res.*, *110*, B09406, doi:10.1029/2004JB003338.

Gao, J., et al. (2002), Rupture characteristics of the Zhangbei earthquake sequence analyzed by exact focal location, *Seismol. Geol.*, *24*, 81–90.

Harris, R. A., and P. Segall (1987), Detection of a locked zone at depth on the Parkfield, California, segment of the San Andreas fault, *J. Geophys. Res.*, *92*, 7945–7962, doi:10.1029/JB092iB08p07945.

Jónsson, S. (2002), Modeling volcano and earthquake deformation from satellite radar interferometric observations, Ph.D. thesis, 174 pp., Stanford University, Stanford, Calif.

Jónsson, S., H. Zebker, P. Segall, and F. Amelung (2002), Fault slip distribution of the Mw 7.1 Hector Mine earthquake, California, estimated from satellite radar and GPS measurements, *Bull. Seismol. Soc. Am.*, *92*, 1377–1389, doi:10.1785/0120000922.

Lai, X., G. Diao, and Z. Shun (2007), The study on seismogenic structure of Zhangbei earthquake using near field aftershock observation data, *Prog. Geophys.*, *22*, 63–67.

Li, Z., J. Liu, and C. Xu (2004), Error analysis in InSAR data processing (in Chinese), *Geomat. Inf. Sci. Wuhan Univ.*, *29*, 72–76.

Li, Z., J.-P. Muller, P. Cross, and E. J. Fielding (2005), Interferometric synthetic aperture radar (InSAR) atmospheric correction: GPS, Moderate Resolution Imaging Spectroradiometer (MODIS), and InSAR integration, *J. Geophys. Res.*, *110*, B03410, doi:10.1029/2004JB003446.

Li, Z., E. J. Fielding, P. Cross, and J.-P. Muller (2006a), Interferometric synthetic aperture radar atmospheric correction: GPS topography-dependent turbulence model, *J. Geophys. Res.*, *111*, B02404, doi:10.1029/2005JB003711.

Li, Z., E. J. Fielding, P. Cross, and J.-P. Muller (2006b), Interferometric synthetic aperture radar atmospheric correction: Medium Resolution Imaging Spectrometer and Advanced Synthetic Aperture Radar integration, *Geophys. Res. Lett.*, *33*, L06816, doi:10.1029/2005GL025299.

Lin, A., G. Zhao, G. Zhao, and X. Xu (1999), Inferred seismic fault associated with the 1998 M = 6.2 Zhangbei-Shangyi earthquake, Hebei Province, China, *Bull. Seismol. Soc. Am.*, *89*, 550–554.

Lohman, R. B., and M. Simons (2005), Locations of selected small earthquakes in the Zagros mountains, *Geochem. Geophys. Geosyst.*, *6*, Q03001, doi:10.1029/2004GC000849.

Massonnet, D., and K. L. Feigl (1998), Radar interferometry and its application to changes in the Earth's surface, *Rev. Geophys.*, *36*, 441–500, doi:10.1029/97RG03139.

Okada, Y. (1985), Surface deformation due to shear and tensile faults in a half-space, *Bull. Seismol. Soc. Am.*, *75*, 1135–1154.

Rosen, P. A., S. Hensley, G. Peltzer, and M. Simons (2004), Updated repeat orbit interferometry package released, *Eos Trans. AGU*, *85*(47), doi:10.1029/2004EO050004.

Scharroo, R., and P. Visser (1998), Precise orbit determination and gravity field improvement for the ERS satellites, *J. Geophys. Res.*, *103*, 8113–8127, doi:10.1029/97JC03179.

Segall, P., and R. A. Harris (1987), The earthquake deformation cycle on the San Andreas fault near Parkfield, California, *J. Geophys. Res.*, *92*, 10,511–10,525, doi:10.1029/JB092iB10p10511.

Shan, X., J. Ma, X. Song, C. Wang, J. Liu, and G. Zhang (2002), Using deformation field obtained by spaceborne D2INSAR technique to research characteristics of source rupture of Zhangbei-Shangyi earthquake, *Earthquake Res. China*, *18*, 119–126.

Sibthorpe, A. J. (2006), Precision non-conservative force modelling for low Earth orbiting spacecraft, Ph.D. thesis, 260 pp., Univ. College London, London.

Wang, C., Z. Liu, H. Zhang, and X. Shan (2000), The coseismic displacement field of the Zhangbei-Shangyi earthquake mapped by differential radar interferometry, (in Chinese), *Chin. Sci. Bull.*, *45*, 2550–2554.

Wang, Q., et al. (2001), Present-day crustal deformation in China constrained by Global Positioning System measurements, *Science*, *294*, 574–577, PubMed, doi:10.1126/science.1063647.

Wessel, P., and W. H. F. Smith (1998), New, improved version of the Generic Mapping Tools released, *Eos Trans. AGU*, *79*, 579, doi:10.1029/98EO00426.

Wright, T. J., B. E. Parsons, J. A. Jackson, M. Haynes, E. J. Fielding, P. C. England, and P. J. Clarke (1999), Source parameters of the 1 October Dinar (Turkey) earthquake from SAR interferometry and seismic bodywave modelling, *Earth Planet. Sci. Lett.*, *172*, 23–37, doi:10.1016/S0012-821X(99)00186-7.

Wright, T. J., Z. Lu, and C. Wicks (2003), Source model for the $M_w$ 6.7, 23 October 2002, Nenana Mountain Earthquake (Alaska) from InSAR, *Geophys. Res. Lett.*, *30*(18), 1974, doi:10.1029/2003GL018014.

Xu, X., Y. Ran, B. Zhou, G. Yin, J. Li, and W. Liu (1998), Seismotectonics and macrodamage features of the Zhangbei-Shangyi earthquake, *Seismol. Geol.*, *20*, 134–144.

Zhang, H., C. Wang, X. Shan, J. Ma, Y. Tang, and Z. Guo (2001), Focal mechanism analysis and parameter estimation of Zhangbei-Shangyi earthquake from differential SAR interferometry, (in Chinese), *Chin. Sci. Bull.*, *46*, 1837–1840.

Zhang, H., C. Wang, X. Shan, J. Ma, Y. Tang, and Z. Guo (2002), Focal mechanism analysis and parameter estimation of Zhangbei-Shangyi earthquake from differential SAR interferometry, *Chin. Sci. Bull.*, *47*, 334–336, doi:10.1360/02tb9080.